



# Observations of Reconnection Flows in a Flare on the Solar Disk

Juntao Wang , P. J. A. Simões , N. L. S. Jeffrey , L. Fletcher , P. J. Wright , and I. G. Hannah

SUPA, School of Physics and Astronomy, University of Glasgow, Glasgow G12 8QQ, UK; [j.wang.4@research.gla.ac.uk](mailto:j.wang.4@research.gla.ac.uk)

Received 2017 May 30; revised 2017 August 27; accepted 2017 August 29; published 2017 September 13

## Abstract

Magnetic reconnection is a well-accepted part of the theory of solar eruptive events, though the evidence is still circumstantial. Intrinsic to the reconnection picture of a solar eruptive event, particularly in the standard model for two-ribbon flares (CSHKP model), are an advective flow of magnetized plasma into the reconnection region, expansion of field above the reconnection region as a flux rope erupts, retraction of heated post-reconnection loops, and downflows of cooling plasma along those loops. We report on a unique set of *Solar Dynamics Observatory*/Atmospheric Imaging Assembly imaging and *Hinode*/EUV Imaging Spectrometer spectroscopic observations of the disk flare SOL2016-03-23T03:54 in which all four flows are present simultaneously. This includes spectroscopic evidence for a plasma upflow in association with large-scale expanding closed inflow field. The reconnection inflows are symmetric, and consistent with fast reconnection, and the post-reconnection loops show a clear cooling and deceleration as they retract. Observations of coronal reconnection flows are still rare, and most events are observed at the solar limb, obscured by complex foregrounds, making their relationship to the flare ribbons, cusp field, and arcades formed in the lower atmosphere difficult to interpret. The disk location and favorable perspective of this event have removed these ambiguities giving a clear picture of the reconnection dynamics.

**Key words:** solar wind – Sun: corona – Sun: coronal mass ejections (CMEs) – Sun: filaments, prominences – Sun: flares – Sun: UV radiation

**Supporting material:** animation

## 1. Introduction

Solar eruptive events, flares, and associated coronal mass ejections are attributed to the liberation of free magnetic energy stored in the corona, possibly due to magnetohydrodynamic (MHD) instabilities and magnetic reconnection. The “CSHKP” model is the standard 2D framework for two-ribbon flares (Carmichael 1964; Sturrock 1966; Hirayama 1974; Kopp & Pneuman 1976) and predicts several different flows in the flare corona. There is an inflow of plasma and magnetic field toward a diffusion region where reconnection occurs and an outflow from this region of newly reconnected field retracting due to magnetic tension. Both flows are (roughly) perpendicular to the magnetic field direction. There is cooling, condensing material flowing along post-reconnection loops down toward the solar surface. The flare or eruption may influence the ubiquitous upflows at the edge of the active region (AR). In this Letter, we show that a plasma upflow parallel to the inflow field may also happen as the field erupts.

Evidence for reconnection inflows has been reported in a handful of flares, mainly at the solar limb. Yokoyama et al. (2001) reported the first clear extreme-ultraviolet (EUV) inflow following an eruption, with a bright cusp—another ingredient in the CSHKP model—seen underneath in soft X-rays (SXR). Narukage & Shibata (2006) found a further six limb inflow events in nearly five years of Extreme-ultraviolet Imaging Telescope (EIT) observations. A bright, elongated structure in the inflow convergence region was claimed by Lin et al. (2005) to be a current sheet, and the features flowing up along it to be

reconnection outflows. A few more inflows have been reported using observations from the Atmospheric Imaging Assembly (AIA; Lemen et al. 2012) on board the *Solar Dynamics Observatory* (SDO; Pesnell et al. 2012). Savage et al. (2012) studied an inflow with speed up to  $\sim 300 \text{ km s}^{-1}$  in an impulsive flare, while other reports, usually of long-duration events have speeds below  $\sim 100 \text{ km s}^{-1}$ . Sun et al. (2015) reported groups of inflowing “threads” with plasma heating where they make contact, but without a clear hot cusp. In three different flares, Su et al. (2013), Yang et al. (2015), and Zhu et al. (2016) observed a reconnection inflow with two sets of closed loops approaching each other—a different geometry from the standard model.

Reconnection outflows—the retraction of post-reconnection magnetic loops—have occasionally been reported in SXR limb flares (Forbes & Acton 1996; Reeves et al. 2008), but EUV is better at picking out retracting structures. Liu et al. (2013) detected many individual retracting loops in AIA 131 Å observations of a limb flare, with speeds from tens to hundreds of  $\text{km s}^{-1}$ . Imada et al. (2013) combined AIA and *Hinode* EUV Imaging Spectrometer (EIS; Culhane et al. 2007) observations to infer that the hot reconnected loops  $\sim 30 \text{ MK}$  could shrink at a speed above  $500 \text{ km s}^{-1}$ . Supra-arcade downflows, the dark voids in EUV and SXR observations appearing high in the corona and traveling down at tens to hundreds of  $\text{km s}^{-1}$ , are interpreted as the cross-sections of underdense, retracting post-reconnection loops, or the “wakes” left as they descend (e.g., McKenzie & Hudson 1999). Plasma draining in flare loops has also been observed (e.g., Savage et al. 2012). EIS spectroscopic observations show that the draining speed along AR loops at quiescent stage (when there is no flare or eruption) is around tens of  $\text{km s}^{-1}$  (Del Zanna 2008; Syntelis et al. 2012).



Original content from this work may be used under the terms of the [Creative Commons Attribution 3.0 licence](https://creativecommons.org/licenses/by/3.0/). Any further distribution of this work must maintain attribution to the author(s) and the title of the work, journal citation and DOI.

The inflow Alfvén Mach number defining the reconnection rate for these events is estimated at  $\sim 10^{-1}$ – $10^{-3}$  in the fast reconnection regime (the slow Sweet-Parker rate is  $\sim 10^{-4}$ – $10^{-6}$  for typical coronal conditions; Aschwanden 2005). But a good estimate of the reconnection rate requires knowledge of the coronal magnetic field strength, which is difficult to obtain in the limb events stated above. Their position also makes the relationship between cusp loops and footpoints hard to ascertain as the footpoints are usually obscured by the solar limb or complex foreground structures.

We report here on a long-lasting reconnection event near the disk center, focusing on its flow processes and magnetic reconnection rate. Li et al. (2017) studied this event using *SDO/AIA*, demonstrating the relationship between the erupting flux rope and magnetic reconnection, and the transition from 3D to 2D reconnection. The event’s location and quasi-2D geometry in the late phase permit a good estimate of the coronal Alfvén speed and reconnection rate. It exhibits the norms of the standard CSHKP model, with a well-formed cusp underneath inflow threads that can be mapped well to their lower-atmosphere counterparts. The field below the cusp contracts and cools (though the brightest portion rises). We also find spectroscopic evidence for a new kind of plasma upflow associated with the expanding but closed inflow field during a flare, distinct from the common plasma upflows at the AR boundary at the quiescent stage that have been reported by previous authors.

## 2. Observations and Analyses

### 2.1. Instruments and Data Reduction

SOL2016-03-23T03:54 was a *Geostationary Operational Environmental Satellite (GOES)* class C1.1 flare in AR NOAA 12524 (N15W16). We study it from  $\sim 01:00$  UT to  $\sim 07:00$  UT. The *SDO/AIA* and Helioseismic and Magnetic Imager (HMI; Schou et al. 2012) provide EUV images and photospheric magnetograms, respectively, that have been processed using standard software (Boerner et al. 2012) and rotated to 01:00 UT. The EIS on *Hinode* observes the AR in a slow raster from 04:01:50 UT to 05:02:42 UT with a  $1''$  slit moving around every minute from solar west to east over a field of view  $119''.8 \times 512''.0$ . Line-of-sight velocities are obtained from Fe XII and Fe XIII lines, which are intense and also visible outside the AR, for estimating a reliable rest wavelength. Standard EIS data reduction procedures were used, and the spectral lines were fitted with single Gaussians. The rest wavelength was extracted from a quiet-Sun region  $X \sim (-24'', 85'')$  and  $Y \sim (157'', 207'')$  (excluding missing values along a vertical data gap at  $X \sim 13''$ ) free of AR emission. The upper-limit uncertainty is  $\sim 5 \text{ km s}^{-1}$  for both Fe XII 195.12 Å and Fe XIII 202.04 Å, and Fe XVI 262.98 Å has an upper-limit uncertainty of  $\sim 9 \text{ km s}^{-1}$ . The alignment between AIA and EIS is conducted by eye and also takes Fe IX 197.86 Å into account (but Fe IX intensity is too low for reliable Doppler velocity diagnostics). Fe IX is aligned with 171 Å, Fe XII with 193 Å, Fe XIII with 211 Å, and Fe XVI with 335 Å, as their characteristic temperatures are comparable separately. The accuracy of the alignment is  $\sim 1''$ – $2''$ .

### 2.2. Evolution of the Flare

Figure 1 shows the overall evolution of the flare. Before the flare (Figure 1(a)) a large arcade of loops in 171 Å envelopes a

dark void underneath, possibly a flux rope (Li et al. 2017). Between the arcade footpoints a filament can vaguely be seen (Figures 1(b) and (e) show the filament more clearly). In Figure 1(b), the two ends of the filament suddenly brighten (microflare), accompanied by a small ejection to the north. This may show the destabilization of the hosted flux rope, leading to the subsequent arcade eruption in Figure 1(c). As the arcade erupts, its legs converge, forming a dark cusp underneath in 171 Å, shown in Figure 1(d). The flare ensues with a bright cusp in 131 Å (red) inside the dark cusp in 171 Å. Then two ribbons sweep across the footpoints of the bright cusp and separate away from the filament, seen in 304 Å in Figure 1(e). Figure 1(f) shows the post-flare state with flaring loops appearing in 171 Å. The main evolution from Figures 1(a), (c), (d), and (f) reveals that the correspondence between the pre-flare arcade, the erupting arcade, the bright cusp, and the flaring loops is well established in terms of their footpoint locations, indicated by the two magenta circles. Figures 2(a)–(c) show the time slices corresponding to cuts 1–3 in Figure 1, respectively. A light curve in 304 Å for the microflare in Figure 1(b) is added in Figure 2(c) and the *GOES* SXR light curves in Figure 2(d). The vertical dotted line “A” indicates the timing of the microflare and the arcade eruption and line “B” the timing of the inflow and the flare. Different flows are discussed in the following paragraphs.

### 2.3. Flows in the Flare

**Reconnection Inflows**—Figure 2(a) shows the evolution along cut 1 through the flare cusp region. Before the flare, the threads forming the arcade legs separate as the flux rope erupts. The threads then accelerate toward the (presumed) central diffusion region, approaching with projected speeds of tens of  $\text{km s}^{-1}$ , similar on either side. These are fitted with exponential equations by picking a few points along specific inflow features and extrapolated to the diffusion regions indicated by the cyan boxes. The speeds at the final times of the fit curves are larger than those in Li et al. (2017) because we choose a cut with a higher altitude than theirs, closer to the reconnection site at 03:50 UT in Figure 1(d), in order to account for the progressively higher up reconnection site. Accelerated inflows were also found by Sun et al. (2015) and Zhu et al. (2016). After the *GOES* peak, the western leg gradually fades, while the flow of the outer threads of the eastern leg starts to decelerate toward the central region, reducing to a few  $\text{km s}^{-1}$ . Figure 2(c) shows the corresponding ribbon separation, also with similar speed on each side.

**Reconnection Outflows**—The post-reconnection outflow is manifested as a contraction of the loops underneath the cusp, visible as bright and dark striations in the stackplot (Figure 2(b)) of superposed 131 Å and 94 Å slices, on a linear intensity scale, along cut 2 vertically down through the cusp loops (also can be seen in the reference image of Figure 2(d) on a logarithmic intensity scale in 131 Å). The yellow dashed line in Figure 2(b) shows the looptop in the cusp declining in altitude with time, illustrating the contraction of the cusp loops. The contraction decelerates with time, while the loops also cool down from 131 Å ( $\sim 10$  MK) to 94 Å ( $\sim 6.8$  MK). This is not well observed in the past to our knowledge. Meanwhile, the brightest portion of the cusp rises, as expected if the reconnection site progressively moves upward. We note the qualitative similarity between the observed trajectories of

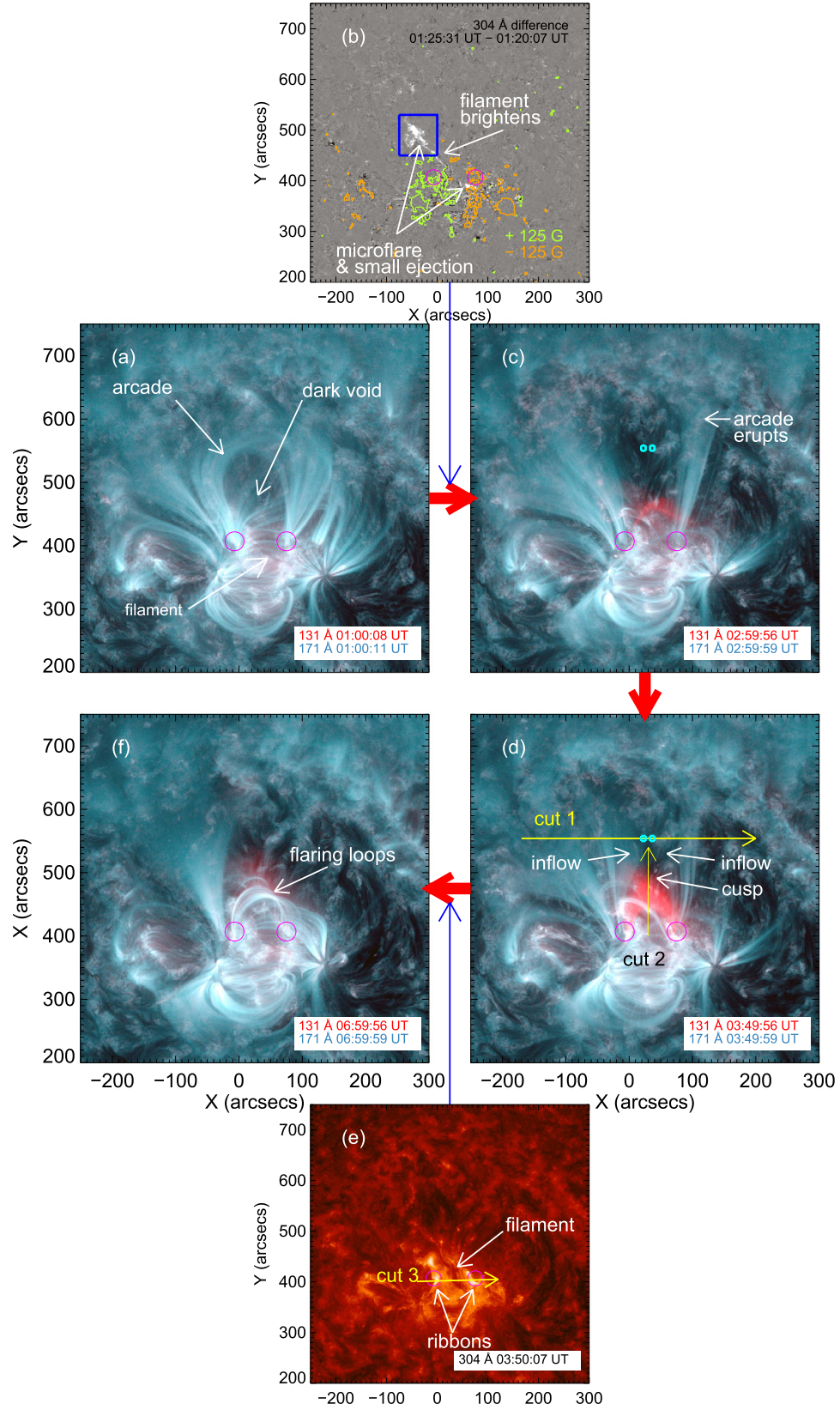


**Figure 1.** Evolution of the flare. Panels (a), (c), (d), and (f) show the main evolution sequence in composite AIA 131 Å and 171 Å images. (b) The microflare and small ejection in the 304 Å difference image just before the arcade eruption. The HMI magnetogram contours at  $\pm 125$  G are overlaid. The blue rectangle is used for the light curve in Figure 2(c). (e) The ribbon separation in 304 Å. The magenta circles in each image show the relevant footpoint locations. Cuts 1–3 are used for time slices in Figures 2(a)–(c), respectively. The two cyan boxes in panels (c) and (d) are for DEM analysis in Section 2.4.

(An animation of this figure is available.)



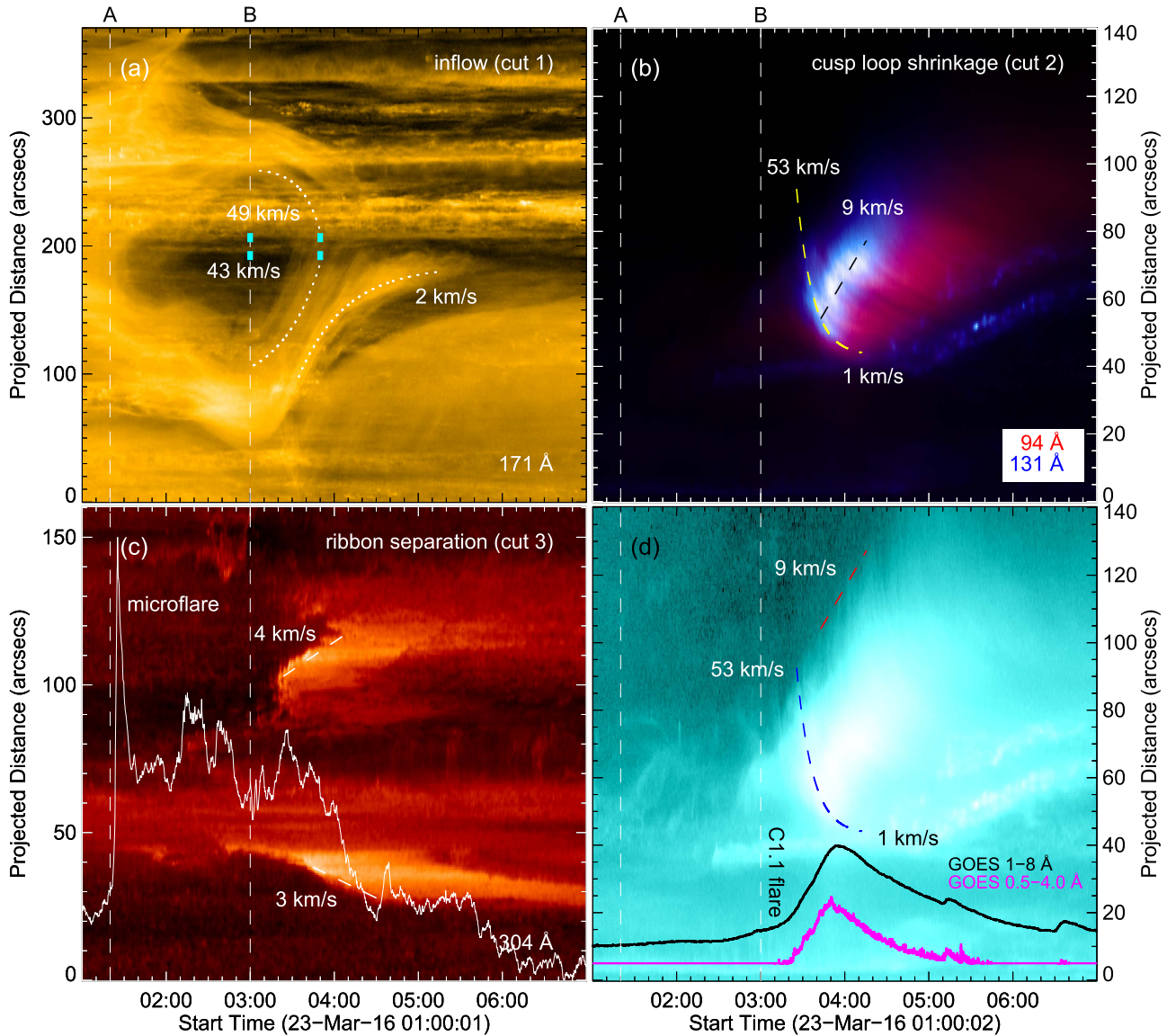


**Figure 2.** (a) Time slice of cut 1 for the evolution of the inflow threads. The two cyan boxes at 03:00 UT and also 03:50 UT show the positions used for DEM analysis in Section 2.4, as in Figures 1(c) and (d). The speeds given are for the final times of the fit curves. (b) Time slice of cut 2 combines 94 Å and 131 Å on a linear intensity scale, showing the evolution of the bright cusp. Its corresponding image on a logarithmic intensity scale in 131 Å is plotted in panel (d). The yellow dashed fit curve is the same as the blue one in panel (d), and the black dashed fit curve is the same as the red one in panel (d) but moved downward to match the brightest portion. (c) Time slice of cut 3 for the evolution of the ribbons. The light curve in 304 Å of the microflare indicated in Figure 1(b) is overlaid. (d) GOES SXR light curves overlaid on the time slice image of cut 2 in 131 Å on a logarithmic intensity scale for reference. The dotted line A denotes the timings of the arcade eruption and the microflare and B the timings of the inflow and the C1.1 flare.

the contracting loops and those calculated by Lin (2004) for a 2D reconnecting current sheet model.

**Plasma downflows**—Figures 3(a) and (c) show the Fe XVI and Fe XIII intensity maps from EIS, and Figures 3(b) and (d) show the corresponding line-of-sight velocity maps. For comparison, Figures 3(e) and (f) are synthesized AIA “raster” images that simulate the EIS slit scanning mode, produced by combining narrow slices of AIA images at the EIS slit locations and times. Looptops and loop legs of the flare arcades (Figures 3(b) or (d)) have redshifts of  $\sim 13 \text{ km s}^{-1}$  indicating plasma draining, or loop contraction. We consider plasma draining to be the more likely explanation as the line-of-sight speed is much larger than the projected contraction speed  $\sim 1 \text{ km s}^{-1}$  obtained from the hotter 94 Å observations at that

time (Figure 2(b)). An interpretation in terms of contraction is thus difficult to reconcile with the observed arcade geometry.

**Plasma upflows**—We also have evidence of plasma upflows at the edge of the AR. The strong blueshift  $\sim 25 \text{ km s}^{-1}$  at the eastern footpoint of the cusp (at  $(X, Y) \sim (25'', 400'')$  in Figures 3(b) and (d)) could indicate chromospheric evaporation onto the reconnected cusp field (Figures 3(a) and (e)). Just to its east is an extended blueshift area (enclosed by the yellow dashed line at the bottom left corner in Figure 3(d)). This area can be divided into three parts: the strongest blueshift feature indicated by the magenta dotted line, the “E” region to the east, and the “W” region to the west. The W region possesses stronger blueshift than the E region. Note that the strongest blueshift feature in this area is well aligned with the gap with weak emission in the composite

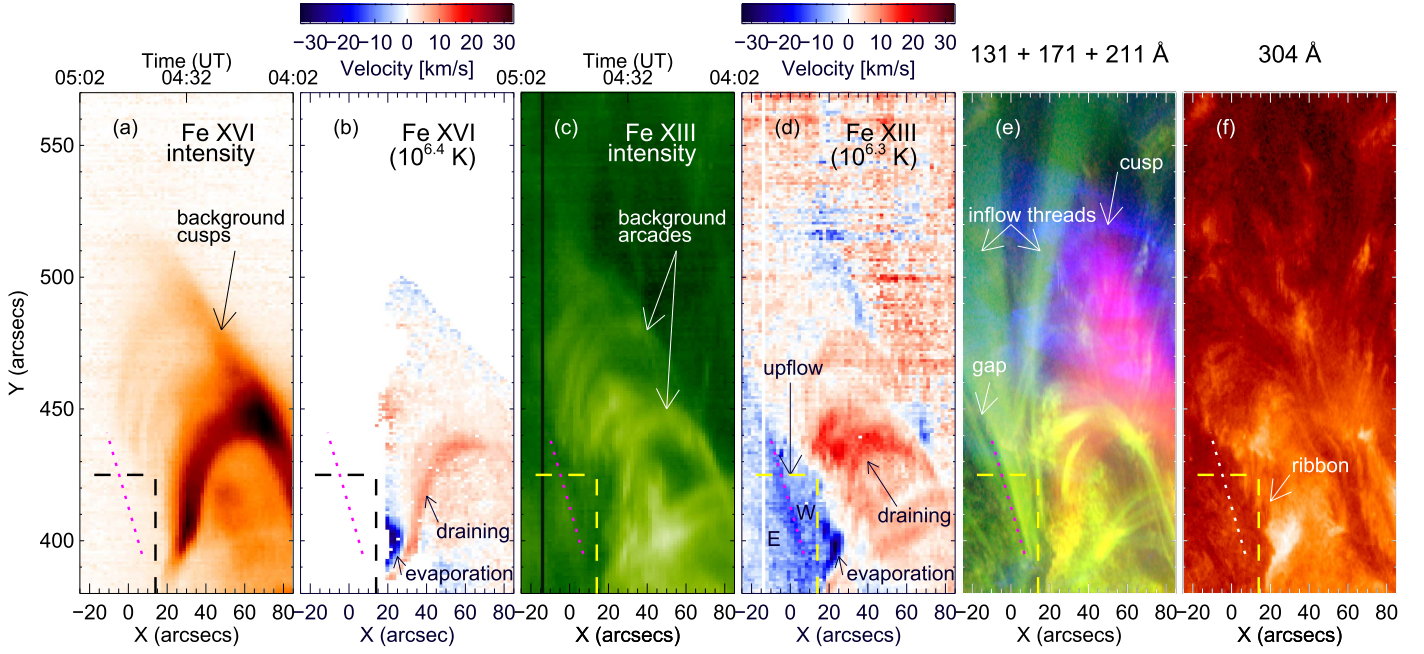


**Figure 3.** ((a), (b)) Fe XVI 262.98 Å intensity and Doppler velocity maps. ((c), (d)) Fe XIII 202.04 Å intensity and Doppler velocity maps (Fe XII 195.12 Å intensity and Doppler velocity maps are not shown here as they are similar to the ones of Fe XIII). The sampling times of the EIS slit are added above ((a), (c)). ((e), (f)) Synthesized AIA images simulating the EIS slit scanning mode for comparison. 131 Å is red, 171 Å green, and 211 Å blue in panel (e). To align with EIS observations, they have not been rotated like in Figure 1. The dashed line at the bottom left corner encloses the extended blueshift area in panel (d). The magenta dotted line is for the longitudinal velocity profiles in Figure 4.

AIA image in Figure 3(e), which boosts our confidence in the accuracy of the alignment between EIS and AIA.

By comparing Figure 3(d) with Figure 3(e), it can be seen that the field corresponding to this extended blueshift area has not yet been reconnected in the main flare related to the bright cusp, so the blueshifts cannot be explained by the evaporation from the main flare. Nor can they be attributed to evaporation in the background, as the 304 Å ribbon in Figure 3(f) has not reached this area. For the strongest blueshift feature indicated by the magenta line, which is just to the east of the edge of the inflow threads, we can also exclude it being due to changing field inclination. If the line-of-sight velocity profiles along the dotted line, shown in Figure 4, were completely due to the inflow threads inclining toward us, we would expect a blueshift around zero at the footpoints and increasing with altitude. The observation in Figure 4 contradicts this. Figure 4 also excludes a loop siphon flow, in which the flows accelerate toward higher altitudes (Aschwanden 2005). An easy way to interpret the blueshift along the dotted line is to invoke a plasma upflow along a field that inclines toward us. The same argument also applies to the W region. For the E region, it is difficult to argue as the velocity values are comparable to the rest wavelength uncertainty.

#### 2.4. Electron Density Estimate

Differential emission measure (DEM) analysis can be used to estimate the electron density  $n_e$  (Hannah & Kontar 2013). The DEM is defined as  $\xi(T) = n_e^2 dl/dT$  (Craig & Brown 1976), and integrating over  $T$  results in the emission measure along the line-of-sight  $EM = \int \xi(T) dT = \int n_e^2 dl$ .

We calculate the emission measure during ( $EM_{fl}$  at 03:50 UT) and before ( $EM_{pre}$  at 03:00 UT) the inflow, using the regularization method of Hannah & Kontar (2012) to recover  $\xi(T)$  from the mean intensity in each of the six AIA wavebands (94, 131, 171, 193, 211, 335 Å) with single exposures for both

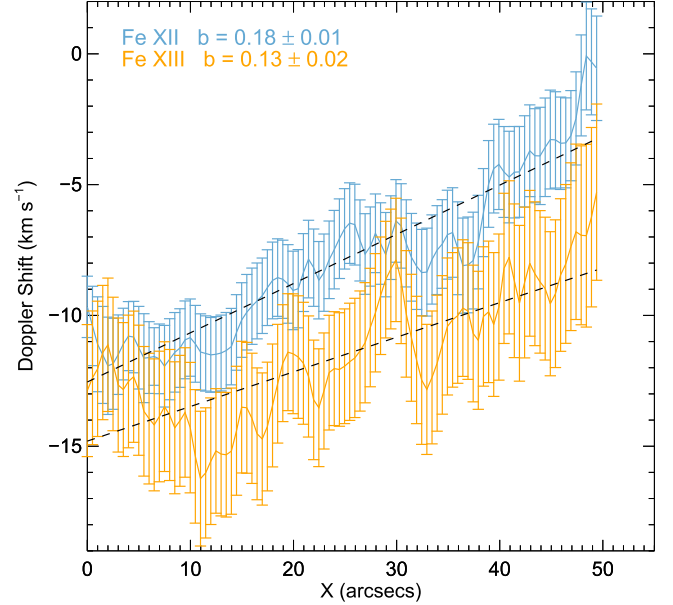


**Figure 4.** Longitudinal velocity profiles for Fe XII and Fe XIII along the dotted line in Figure 3. The origin of the X axis represents the bottom of the dotted line. The dashed line is the linear fit for each profile. “b” represents the slope of the fit and its  $1 - \sigma$  uncertainty. The uncertainty for the rest wavelength estimation is  $\sim 5 \text{ km s}^{-1}$  for both lines, which would shift the entire profiles up or down.

the eastern and western inflow regions (the two cyan boxes in Figures 1(c) and (d)). The temperature range used as input is  $10^{5.5} - 10^{6.6} \text{ K}$ . The resulting DEM enhancement caused by the inflow concentrates between  $10^{5.8}$  and  $10^{6.3} \text{ K}$ , consistent with AIA observations, as the inflow threads can be most clearly seen in AIA 171 Å, which is more sensitive to this temperature range compared to other filters. However, the resulting EMs also contain a contribution from the background and

**Table 1**  
Magnetic Reconnection Parameters

Region	$V_{\text{patt}}^{\text{a}}$ (km s <sup>-1</sup> )	$V_{\text{xp}}^{\text{b}}$ (km s <sup>-1</sup> )	$\theta^{\text{c}}$ (°)	$V_{\text{in}}^{\text{d}}$ (km s <sup>-1</sup> )	$V_{\text{foot}}^{\text{e}}$ (km s <sup>-1</sup> )	$B_{\text{foot}}^{\text{f}}$ (G)	$B_{\text{in}}^{\text{g}}$ (G)	$\text{EM}_{\text{in}}^{\text{h}}$ (10 <sup>25</sup> cm <sup>-5</sup> )	$L^{\text{i}}$ arcsec	$n_e^{\text{j}}$ (10 <sup>8</sup> cm <sup>-3</sup> )	$V_A^{\text{k}}$ (km s <sup>-1</sup> )	$M_A^{\text{l}}$
Eastern	43	9	27	38	3	131	10	4.8	15	2.1	1371	0.03
Western	49	9	27	44	4	-125	11	4.3	15	2.0	1551	0.03

**Notes.** These estimates are made at ~03:50 UT, just before the *GOES* 1–8 Å flux peaks. The method for estimating the reconnection rate  $M_A$  in the last column is described in Section 2.5.

<sup>a</sup> Obtained from Figure 2(a).

<sup>b</sup> Estimated from the rising speed of the bright cusp in 131 Å in Figures 2(b) and (d).

<sup>c</sup> Estimated at half the angle of the dark cusp in 171 Å in Figure 1(d).

<sup>d</sup> Via Equation (4).

<sup>e</sup> From Figure 2(c).

<sup>f</sup> Approximated as the mean of the HMI longitudinal magnetic strength above a noise level ~10 G (Liu et al. 2012) for the magenta circles in Figure 1.

<sup>g</sup> Via Equation (6) and transformed to absolutes.

<sup>h</sup> Through the method in Section 2.4.

<sup>i</sup> Approximated as the diameter of the magenta circle in Figure 1.

<sup>j</sup> Via Equation (2).

<sup>k</sup> Through Equation (5).

<sup>l</sup> Via Equation (3) or (7).

foreground corona. If we assume that (i) the background and foreground density outside the inflow threads does not change much during the event, and (ii) the density within the inflow region during the inflow (Figure 1(d)) is much larger than before the inflow (Figure 1(c)), then we can obtain the emission measure of the inflow region  $\text{EM}_{\text{in}}$  by taking

$$\text{EM}_{\text{in}} = \text{EM}_{\text{fl}} - \text{EM}_{\text{pre}}. \quad (1)$$

The electron density of the inflow region can then be estimated by

$$n_e = \sqrt{\text{EM}_{\text{in}}/L}, \quad (2)$$

with  $L$  being the line-of-sight thickness of the inflow region.

As  $n_e \propto L^{-0.5}$  in Equation (2), the estimated density is not very sensitive to the choice of the thickness  $L$ . Thus, we choose the diameter of the magenta circle in Figure 1 as an approximation of the thickness of the inflow threads,  $L = 15$  arcsec  $\approx 1.1 \times 10^9$  cm. We then find  $n_e \approx 2.1 \times 10^8$  cm<sup>-3</sup> and  $\approx 2.0 \times 10^8$  cm<sup>-3</sup> for the eastern and western regions, respectively (Table 1).

Assumption (i) above seems reasonable as no obvious events (except the inflow) happen during this period along the chosen boxes' line of sight. Assumption (ii) could be true, as first in the pre-inflow stage the two boxes are located within the dark void region (Figure 1(c)), which means a lack of emitting plasma, and second the void expansion may further evacuate the plasma there. And the obtained results above are consistent with EIS density diagnostics using Fe XIII 202.04 and 203.83 Å pair ( $\approx 1.5 \times 10^8$  cm<sup>-3</sup>) around the same regions, though the EIS sampling time is after 04:00 UT (as can be seen in Figure 3) and the reconnection site has already moved upward.

### 2.5. Magnetic Reconnection Rate

The magnetic reconnection rate can be represented by the inflow Alfvén Mach number

$$M_A = V_{\text{in}}/V_A, \quad (3)$$

where  $V_{\text{in}}$  is the inflow speed and  $V_A$  the local Alfvén speed.  $V_{\text{in}}$  can be estimated using

$$V_{\text{in}} = V_{\text{patt}} - V_{\text{xp}} \tan \theta, \quad (4)$$

as in Yokoyama et al. (2001), where  $V_{\text{patt}}$  is the apparent inflow speed obtained from the pattern of inflowing threads,  $V_{\text{xp}}$  the rising speed of the reconnection X-point, and  $\theta$  the angle between the inflow threads and the rising direction of the X-point. This equation accounts for the rising motion of the reconnection site. The Alfvén speed  $V_A$  is

$$V_A = \frac{B_{\text{in}}}{\sqrt{4\pi\rho}} \approx \frac{B_{\text{in}}}{\sqrt{4\pi\mu m_{\text{H}} n_e}} \quad (5)$$

in Gauss units, where  $B_{\text{in}}$  is the magnetic field strength in the inflow region,  $\rho$  the mass density,  $\mu$  the mean atomic weight ( $\sim 1.27$  for coronal abundances; Aschwanden 2005),  $m_{\text{H}}$  the hydrogen mass, and  $n_e$  the electron number density. To obtain  $B_{\text{in}}$ , conservation of magnetic flux can be exploited (e.g., Isobe et al. 2002),

$$B_{\text{in}} V_{\text{in}} = B_{\text{foot}} V_{\text{foot}}, \quad (6)$$

where  $B_{\text{foot}}$  is the vertical magnetic strength at the photosphere and  $V_{\text{foot}}$  the separation speed of flaring ribbons. As this AR is close to the solar disk center, HMI longitudinal magnetograms can be used as a good approximation of the vertical field. By combining Equations (3)–(6), the final equation for the reconnection rate is

$$M_A = \frac{(V_{\text{patt}} - V_{\text{xp}} \tan \theta)^2}{B_{\text{foot}} V_{\text{foot}}} \sqrt{4\pi\mu m_{\text{H}} n_e}, \quad (7)$$

where the electron number density can be estimated as in Section 2.4, and other quantities are obtained as described in the notes to Table 1. The resulting reconnection rates are 0.03 for both the eastern and western inflows.

### 3. Discussion and Conclusions

We have reported the first comprehensive observations of reconnection flows on the solar disk. Threads or strands of



plasma accelerate and later decelerate toward a presumed reconnection site, below which a well-defined hot cusp forms, anchored at the threads' endpoints. Individual cusp loops shrink and cool as the brightest portion of the cusp ascends. The magnetic reconnection rates around the *GOES* flux peak are 0.03 for both the eastern and western inflows, consistent with fast reconnection, and in the range of previous studies (Yokoyama et al. 2001; Lin et al. 2005; Narukage & Shibata 2006; Bemporad et al. 2010; Savage et al. 2012; Su et al. 2013; Sun et al. 2015; Zhu et al. 2016). The reconnection is quite symmetric in this case. According to Equation (7), if  $V_{xp}$  and  $\theta$  are good observational estimates, the reconnection rate estimated is most sensitive to  $V_{patt}$ , only the transverse component of the real inflow velocity. For a rough estimation of the lower limit of the reconnection rate, we double  $B_{foot}$ ,  $V_{foot}$  and reduce  $n_e$  by a factor of 10, giving reconnection rates of around 0.003 for both the eastern and western inflows, which are still in the fast reconnection regime.

There is no emission from the presumed reconnection site; it may be too short or thin, or at the wrong temperature to be detected by the instruments used. We note that the upper part of the dark cusp highlighted in Figure 1(d) is dark in all AIA wavelengths, implying that it has a very low density or temperature above the  $\sim 10$  MK at which the AIA 131 Å filter peaks and where the cusp is clearest.

As argued in Section 2.3, possibilities like evaporation from the main flare, field inclining, and a siphon flow could not be the reasons for the blueshifts along the dotted line and in the W region in Figure 3(d). Plasma upflows along field that inclines toward us could be an explanation for these blueshifts. Blueshift features are found to be ubiquitous at the edge of ARs from EIS observations even in non-flaring regions, persisting from hours to days in areas of weak emission and low density, and possessing velocities around tens of  $\text{km s}^{-1}$ , faster in hotter lines (e.g., Sakao et al. 2007; Del Zanna 2008; Doschek et al. 2008; Harra et al. 2008; Baker et al. 2009; Démoulin et al. 2013; Brooks et al. 2015). They are interpreted as upflows by some authors and considered to be a possible source of the slow solar wind in the heliosphere, but the real origin of these blueshift features is still controversial (Abbo et al. 2016 and references therein).

We here propose a distinction between two upflow components associated with the blueshift features observed in this event. The strongest blueshift in Figure 3(d) is well aligned with the gap with weak AIA emission in Figure 3(e), which may imply an open field short of emitting plasma, while the W region evidently corresponds to the large-scale closed loops that are the inflow threads or the legs of the arcade loops erupting outward<sup>1</sup> in Figure 3(e). The potential-field source-surface (PFSS) model just before the flare in Figure 5 provides supporting evidence. It well reflects the pre-eruption structure seen in Figure 1(a) and shows that the extended blueshift area in Figure 3(d) consists of a mix of open and closed fields. Two closed-field domains are separated by a very narrow open-field corridor, which matches with the structure in the extended blueshift area in Figure 3(d) with the strongest blueshift feature indicated by the dotted line separating the E and W regions apart. Thus, it seems that plasma upflows occur along both open field and large-scale closed loops. The argument above helps solve the long-standing problem of whether the blueshift-related upflows at the AR boundary are associated with open or large-scale closed field (Sakao et al. 2007; Harra et al. 2008;

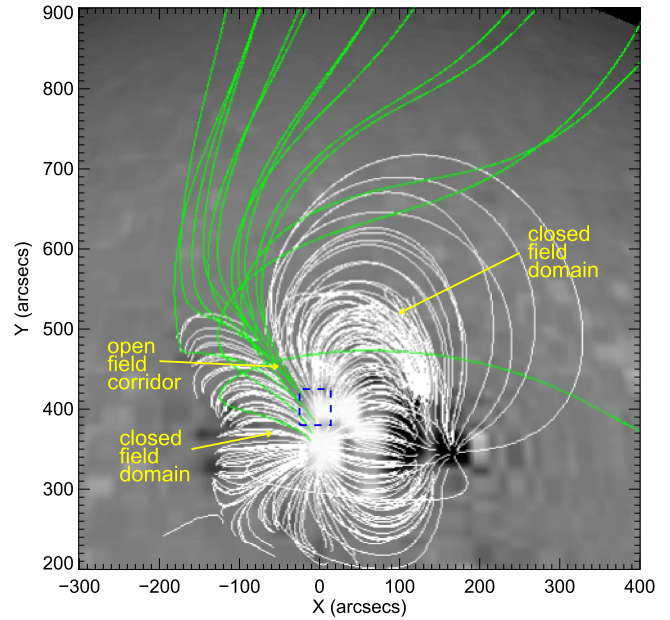


**Figure 5.** Model field at 00:04 UT just before the arcade eruption and the flare, derived from the PFSS package of Solarsoft, whose perspective has been rotated to 04:50 UT in order to compare with the extended blueshift region observed by EIS in Figure 3(d). It shows a narrow open-field corridor between two closed-field domains. The open-field corridor extends northward to a coronal hole. The blue dashed box shows the same region as the bottom left corner enclosed by the dashed line in Figure 3.

Baker et al. 2009; Del Zanna et al. 2011; Boutry et al. 2012; Brooks et al. 2015; Edwards et al. 2016).

As the blueshift levels of the feature indicated by the dotted line in Figure 3(d) and the W region are quite different (collimated and stronger along the dotted line), different mechanisms may be responsible for the associated upflows. For the upflow in the W region, expansion of related large-scale closed loops (Harra et al. 2008) could be an explanation. When the flux tube of the arcade erupts, the plasma within would expand outward and dilute (Reeves et al. 2010, see the third row of their Figure 9), which results in depressurization. We suggest here that the expansion may not be adiabatic, as the depressurization could induce a plasma upflow from the coronal base along the legs of the expanding arcade. A vivid analogy of this depressurization process is the water in a tube being pumped out by rapidly pulling a plunger, or the air being pumped in as the volume of the lung is increased. Both the plasma expansion itself because of the field inflation and the induced upflow due to depressurization could contribute to the blueshift observed along the expanding closed field. As the inflating field is the inflow threads here, the upflow from the bottom of the corona may serve as a way to increase the plasma density advected into the reconnection region or other acceleration regions (e.g., the slow-mode shock), which could help relax the “electron number problem” (Brown & Melrose 1977; Fletcher & Hudson 2008) to some extent. *Fermi* Gamma-ray Burst Monitor (Meegan et al. 2009) observations barely show any hard X-ray emission from this flare (unfortunately, also no observations from the *Reuven Ramaty High Energy Solar Spectroscopic Imager* for this event), implying a very weak requirement for the electron flux. For a major flare, the eruption and arcade expansion could be more violent, possibly with a faster upflow and increased electron supply.

<sup>1</sup> The upper part of the inflow threads could be contaminated by the background arcades that have draining plasma.

Antiochos et al. (2011) show narrow open-field corridor maps to separatrices and quasi-separatrix layers (QSLs) in the heliosphere where the magnetic connectivities change dramatically and that they are the natural region for interchange reconnection between open and closed field to take place (Fisk et al. 1999; Fisk 2003). Thus, the upflow associated with the open field here in Figure 5 could be created by reconnection between the open field and the two closed domains nearby, which transports plasma from closed field to open field. Comparing Figures 1(a) with (f), it can be seen that the intensity of the eastern closed domain has a significant decrease during the evolution, while the large-scale loops nearby to the west become more intense, which could mean that an interaction happens between the eastern closed domain and the narrow open-field corridor. The main flare or the arcade eruption observed in the western domain may facilitate or impede the dynamics.

A characteristic inclination angle of the open field in Figure 5 toward us can be obtained from the PFSS model to be  $\sim 45^\circ$ . Figure 3(d) (and also Figure 3(b)) provides the characteristic values of the longitudinal velocities of the blueshift feature indicated by the dotted line, the W region, the evaporation feature, and the plasma draining to be  $\sim 10 \text{ km s}^{-1}$ ,  $\sim 5 \text{ km s}^{-1}$ ,  $\sim 25 \text{ km s}^{-1}$ , and  $\sim 13 \text{ km s}^{-1}$ , respectively. If we assume that all the fields related to the above features incline toward us with roughly the same angle of  $\sim 45^\circ$  as the open field does, the total speeds of the associated plasma flows traveling along these fields can be estimated to be  $\sim 14 \text{ km s}^{-1}$ ,  $\sim 7 \text{ km s}^{-1}$ ,  $\sim 35 \text{ km s}^{-1}$ , and  $\sim 18 \text{ km s}^{-1}$ , respectively. They are all subsonic as the sound speed for a plasma with a temperature  $T_e \sim 2.0 \text{ MK}$  or  $\sim 2.5 \text{ MK}$  (for Fe XIII  $\sim 10^{6.3} \text{ K}$  and Fe XVI  $\sim 10^{6.4} \text{ K}$ , respectively) is  $c_s = 147\sqrt{T_e/1 \text{ MK}} \sim 208 \text{ km s}^{-1}$  or  $\sim 232 \text{ km s}^{-1}$  (Aschwanden 2005). The upflow speeds from a few to tens of  $\text{km s}^{-1}$  at the edge of the AR are consistent with previous EIS observations (Del Zanna 2008). The evaporation speed  $\sim 35 \text{ km s}^{-1}$  is similar to the results also obtained by Milligan & Dennis (2009) for a C-class flare at this temperature range. The plasma draining speed  $\sim 18 \text{ km s}^{-1}$  is comparable to previous results derived from EIS spectroscopy (Del Zanna 2008; Syntelis et al. 2012), though they were measured at the quiet stage of the AR evolution. The plasma draining at these spectral lines may reflect the warm counterpart of the cold coronal rain (e.g., Schrijver 2001; Kamio et al. 2011; Vashalomidze et al. 2015) observed later in 304 Å.

In addition, if we take the field inclination into account when calculating the reconnection rate, this will slightly change the values of  $V_{\text{up}}$  and  $\theta$  in Table 1, but the final reconnection rate around the GOES flux peak will still be close to 0.03 for both the inflow regions and in agreement with fast reconnection.

Together with Li et al. (2017), this work reveals the 2D and 3D aspects of this event. The wealth of diagnostic information on the flows and plasma properties around the reconnection region and at the periphery of the AR can be further used to explore the energetics of the reconnection process and the detailed dynamics of flow evolution, while the availability of HMI vector magnetograms means that the magnetic evolution and plasma flows can be investigated in more detail using magnetic field extrapolations and magnetohydrodynamic simulations.

The authors thank the referees for very helpful comments that significantly improved the quality of the manuscript, and also Hugh Hudson for discussion and comments. L.F., P.J.A.S.,

and N.L.S.J. acknowledge support from STFC Consolidated Grant ST/L000741/1. The research leading to these results has received funding from the European Community's Seventh Framework Programme (FP7/2007-2013) under grant agreement No. 606862 (F-CHROMA). P.J.W. is supported by an EPSRC/Royal Society Fellowship Engagement Award (EP/M00371X/1). I.G.H. acknowledges support of a Royal Society University Research Fellowship. The authors are grateful to NASA/SDO, AIA, HMI, Hinode/EIS, and GOES science teams for data access.

*Facilities:* AIA (SDO), HMI (SDO), EIS (Hinode), GOES.

## ORCID iDs

Juntao Wang  <https://orcid.org/0000-0001-9268-2966>  
 P. J. A. Simões  <https://orcid.org/0000-0002-4819-1884>  
 N. L. S. Jeffrey  <https://orcid.org/0000-0001-6583-1989>  
 L. Fletcher  <https://orcid.org/0000-0001-9315-7899>  
 P. J. Wright  <https://orcid.org/0000-0001-9021-611X>  
 I. G. Hannah  <https://orcid.org/0000-0003-1193-8603>

## References

- Abbo, L., Ofman, L., Antiochos, S. K., et al. 2016, *SSRv*, **201**, 55  
 Antiochos, S. K., Mikić, Z., Titov, V. S., Lionello, R., & Linker, J. A. 2011, *ApJ*, **731**, 112  
 Aschwanden, M. J. 2005, *Physics of the Solar Corona. An Introduction with Problems and Solutions* (2nd ed.; Chichester: Praxis)  
 Baker, D., van Driel-Gesztelyi, L., Mandrini, C. H., Démoulin, P., & Murray, M. J. 2009, *ApJ*, **705**, 926  
 Bemporad, A., Soenen, A., Jacobs, C., Landini, F., & Poedts, S. 2010, *ApJ*, **718**, 251  
 Boerner, P., Edwards, C., Lemen, J., et al. 2012, *SoPh*, **275**, 41  
 Boutry, C., Buchlin, E., Vial, J.-C., & Régnier, S. 2012, *ApJ*, **752**, 13  
 Brooks, D. H., Ugarte-Urra, I., & Warren, H. P. 2015, *NatCo*, **6**, 5947  
 Brown, J. C., & Melrose, D. B. 1977, *SoPh*, **52**, 117  
 Carmichael, H. 1964, *NASSP*, **50**, 451  
 Craig, I. J. D., & Brown, J. C. 1976, *A&A*, **49**, 239  
 Culhane, J. L., Harra, L. K., James, A. M., et al. 2007, *SoPh*, **243**, 19  
 Del Zanna, G. 2008, *A&A*, **481**, L49  
 Del Zanna, G., Aulanier, G., Klein, K.-L., & Török, T. 2011, *A&A*, **526**, A137  
 Démoulin, P., Baker, D., Mandrini, C. H., & van Driel-Gesztelyi, L. 2013, *SoPh*, **283**, 341  
 Doschek, G. A., Warren, H. P., Mariska, J. T., et al. 2008, *ApJ*, **686**, 1362  
 Edwards, S. J., Parnell, C. E., Harra, L. K., Culhane, J. L., & Brooks, D. H. 2016, *SoPh*, **291**, 117  
 Fisk, L. A. 2003, *JGRA*, **108**, 1157  
 Fisk, L. A., Zurbuchen, T. H., & Schwadron, N. A. 1999, *ApJ*, **521**, 868  
 Fletcher, L., & Hudson, H. S. 2008, *ApJ*, **675**, 1645  
 Forbes, T. G., & Acton, L. W. 1996, *ApJ*, **459**, 330  
 Hannah, I. G., & Kontar, E. P. 2012, *A&A*, **539**, A146  
 Hannah, I. G., & Kontar, E. P. 2013, *A&A*, **553**, A10  
 Harra, L. K., Sakao, T., Mandrini, C. H., et al. 2008, *ApJL*, **676**, L147  
 Hirayama, T. 1974, *SoPh*, **34**, 323  
 Imada, S., Aoki, K., Hara, H., et al. 2013, *ApJL*, **776**, L11  
 Isobe, H., Yokoyama, T., Shimojo, M., et al. 2002, *ApJ*, **566**, 528  
 Kamio, S., Peter, H., Curdt, W., & Solanki, S. K. 2011, *A&A*, **532**, A96  
 Kopp, R. A., & Pneuman, G. W. 1976, *SoPh*, **50**, 85  
 Lemen, J. R., Title, A. M., Akin, D. J., et al. 2012, *SoPh*, **275**, 17  
 Li, Y., Sun, X., Ding, M. D., Qiu, J., & Priest, E. R. 2017, *ApJ*, **835**, 190  
 Lin, J. 2004, *SoPh*, **222**, 115  
 Lin, J., Ko, Y.-K., Sui, L., et al. 2005, *ApJ*, **622**, 1251  
 Liu, W., Chen, Q., & Petrosian, V. 2013, *ApJ*, **767**, 168  
 Liu, Y., Hoeksema, J. T., Scherrer, P. H., et al. 2012, *SoPh*, **279**, 295  
 McKenzie, D. E., & Hudson, H. S. 1999, *ApJL*, **519**, L93  
 Meegan, C., Lichti, G., Bhat, P. N., et al. 2009, *ApJ*, **702**, 791  
 Milligan, R. O., & Dennis, B. R. 2009, *ApJ*, **699**, 968  
 Narukage, N., & Shibata, K. 2006, *ApJ*, **637**, 1122  
 Pesnell, W. D., Thompson, B. J., & Chamberlin, P. C. 2012, *SoPh*, **275**, 3  
 Reeves, K. K., Linker, J. A., Mikić, Z., & Forbes, T. G. 2010, *ApJ*, **721**, 1547



- Reeves, K. K., Seaton, D. B., & Forbes, T. G. 2008, [ApJ](#), **675**, 868
- Sakao, T., Kano, R., Narukage, N., et al. 2007, [Sci](#), **318**, 1585
- Savage, S. L., Holman, G., Reeves, K. K., et al. 2012, [ApJ](#), **754**, 13
- Schou, J., Scherrer, P. H., Bush, R. I., et al. 2012, [SoPh](#), **275**, 229
- Schrijver, C. J. 2001, [SoPh](#), **198**, 325
- Sturrock, P. A. 1966, [Natur](#), **211**, 695
- Su, Y., Veronig, A. M., Holman, G. D., et al. 2013, [NatPh](#), **9**, 489
- Sun, J. Q., Cheng, X., Ding, M. D., et al. 2015, [NatCo](#), **6**, 7598
- Syntelis, P., Gontikakis, C., Georgoulis, M. K., Alissandrakis, C. E., & Tsinganos, K. 2012, [SoPh](#), **280**, 475
- Vashalomidze, Z., Kukhianidze, V., Zaqarashvili, T. V., et al. 2015, [A&A](#), **577**, A136
- Yang, S., Zhang, J., & Xiang, Y. 2015, [ApJL](#), **798**, L11
- Yokoyama, T., Akita, K., Morimoto, T., Inoue, K., & Newmark, J. 2001, [ApJL](#), **546**, L69
- Zhu, C., Liu, R., Alexander, D., & McAteer, R. T. J. 2016, [ApJL](#), **821**, L29